**RESEARCH ARTICLE**

# Proximity Effect of Fe–Zn Bimetallic Catalysts on $CO_2$ Hydrogenation Performance

Shengkun Liu[1] · Qiao Zhao[2,3] · Xiaoxue Han[1] · Chongyang Wei[1] · Haoting Liang[1] · Yidan Wang[1] · Shouying Huang[1,3] · Xinbin Ma[1]

**Abstract**
The interaction between a promoter and an active metal crucially impacts catalytic performance. Nowadays, the influence of promoter contents and species has been intensively considered. In this study, we investigate the effect of the iron (Fe)–zinc (Zn) proximity of Fe–Zn bimetallic catalysts on $CO_2$ hydrogenation performance. To eliminate the size effect, $Fe_2O_3$ and ZnO nanoparticles with uniform size are first prepared by the thermal decomposition method. By changing the loading sequence or mixing method, a series of Fe–Zn bimetallic catalysts with different Fe–Zn distances are obtained. Combined with a series of characterization techniques and catalytic performances, Fe–Zn bimetallic proximity for compositions of Fe species is discussed. Furthermore, we observe that a smaller Fe–Zn distance inhibits the reduction and carburization of the Fe species and facilitates the oxidation of carbides. Appropriate proximity of Fe and Zn (i.e., $Fe_1Zn_1$-imp and $Fe_1Zn_1$-mix samples) results in a suitable ratio of the $Fe_5C_2$ and $Fe_3O_4$ phases, simultaneously promoting the reverse water–gas shift and Fischer–Tropsch synthesis reactions. This study provides insight into the proximity effect of bimetallic catalysts on $CO_2$ hydrogenation performance.

**Graphical Abstract**
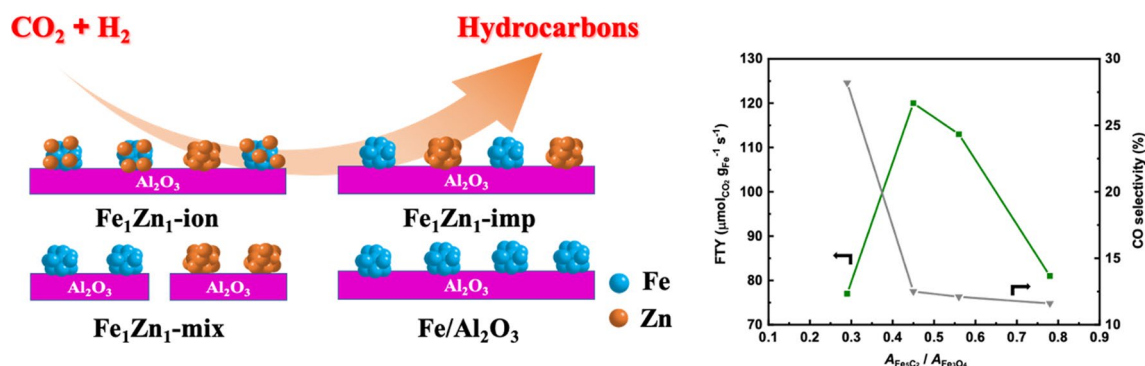


**Keywords** $CO_2$ hydrogenation · Fe-based catalyst · Promoter · Proximity effect

✉ Qiao Zhao
qiaozhao@nankai.edu.cn

✉ Shouying Huang
huangsy@tju.edu.cn

1 Key Laboratory for Green Chemical Technology of Ministry of Education, Haihe Laboratory of Sustainable Chemical Transformations, School of Chemical Engineering and Technology, Tianjin University, Tianjin 300072, China

2 School of Materials Science and Engineering, National Institute for Advanced Materials, Nankai University, Tianjin 300350, China

3 Zhejiang Institute of Tianjin University, Ningbo 315201, China

## Introduction

Excessive emission of $CO_2$ by the use of fossil fuels gives rise to various environmental problems, including global warming, glacier melting, climate change, and ocean acidification [1–3]. However, $CO_2$ can be regarded as an abundant, clean, nontoxic renewable carbon resource. Therefore, converting $CO_2$ into valuable chemicals not only mitigates environmental problems but also reduces dependence on fossil energy [4, 5]. Direct hydrogenation is considered a feasible and promising way for $CO_2$ utilization. Diverse products, such as methanol, syngas, olefins, liquid fuels, and higher alcohols, can be obtained using different catalysts. Fe-based catalysts are a great candidate if the target product is hydrocarbons. Generally, this process involves two steps, the reverse water–gas shift reaction (RWGS) over $Fe_3O_4$ and the Fischer–Tropsch synthesis reaction over iron carbides ($FeC_x$) [6, 7].

To improve the catalytic properties of Fe-based catalysts, promoters are usually introduced to tune the physical and electronic structure of Fe species. Transition metals, such as Mn, Cu, Co, and Zn, have been extensively studied [8–11]. Among them, Zn exhibits versatile promotion effects, such as improving Fe dispersion, catalyzing the RWGS reaction, and tailoring product distribution [12–14]. Ma et al. [15] prepared Zn- and Na-co-modified Fe-based catalysts by coprecipitation and observed that Zn acting as a structure modifier considerably reduced the particle size of Fe species. Zhang et al. [16] introduced a Zn promoter to Fe-based FTS catalysts by microwave–hydrothermal method, which elevated both light olefin selectivity and catalyst stability. This was ascribed to the improved dispersion of Fe phases and decreased carbon deposition. Han's group [17] revealed that ZnO stabilized the active phase ($FeC_x$) in a bimetallic catalyst, thereby suppressing catalyst deactivation. Additionally, Wang et al. [13] observed that in the process of $CO_2$ hydrogenation to olefins, the main role of ZnO was to promote the RWGS reaction. Similarly, Cai et al. [18] revealed that ZnO promoted the RWGS reaction by increasing $CO_2$ adsorption. Furthermore, Zhang et al. [19] discovered that enhanced interaction between Fe and Zn altered the chemical environment of Fe species. The formation of the $ZnFe_2O_4$ solid solution structure inhibited the hydrogenation of olefin intermediates, thereby enhancing the selectivity of lower olefins. Gao et al. [20] revealed that the $FeAlO_x/Fe_5C_2$ structure suppressed C–C coupling and promoted secondary olefin hydrogenation on the $Fe_5C_2$ surface. Following this, the extra addition of Zn would produce a synergistic effect between Zn and Al, which alleviated the undesirably strong interaction between $Fe_5C_2$ and spinel phases, finally improving the $CO_2$ conversion. Han's group [21]

also observed that adding ZnO to Fe-based catalysts contributed to the generation of iron carbide, which enhanced the activity of $CO_2$ hydrogenation to hydrocarbons. Additionally, the decoration of Na into Fe catalysts mainly altered the olefin formation.

The promotion effect of bimetallic catalysts has been discussed from different perspectives. The interaction and intimacy of promoters and active metals are critical in deciding catalytic properties. This study investigates the proximity effect of Fe–Zn bimetallic catalysts on activity and product distribution. $Fe_2O_3$ and ZnO nanoparticles with uniform size are prepared by the thermal decomposition method, and the distance between Fe and Zn is regulated by changing the loading sequences or mixing methods. Combining transmission electron microscopy (TEM), X-ray powder diffraction (XRD), X-ray photoelectron spectroscopy (XPS), $H_2$ temperature-programmed reduction ($H_2$-TPR), Mössbauer spectroscopy, etc., the promotion effect on the evolution of the Fe phase and catalytic properties is detailed.

## Experimental Section

### Chemicals

All chemicals were commercially purchased and directly used, including ferric chloride ($FeCl_3$, Aladdin, 98.0%), zinc chloride ($ZnCl_2$, Aladdin, $\geq 98.0\%$), zinc nitrate hexahydrate ($Zn(NO_3)_2 \cdot 6H_2O$, Aladdin, 99%), sodium oleate ($C_{18}H_{33}NaO_2$, YuanLi Chemical Reagent Co., LTD, AR), oleic acid (Aladdin, $> 90.0\%$), 1-octadecene (Aladdin, $> 90.0\%$), and ethanol and hexane (YuanLi Chemical Reagent Co., LTD, AR). AlOOH·$n$H$_2$O was purchased from Nankai University Catalyst Co. Deionized water was used for catalyst preparation.

### Catalyst Preparation

#### Synthesis of Fe Nanoparticles and Fe/Al$_2$O$_3$ Catalysts

First, Fe nanoparticles were prepared by the thermal decomposition method [22–25]. Specifically, 6.5 g of ferric chloride and 36.5 g of sodium oleate were dissolved into a mixture containing 60 mL of distilled water, 80 mL of ethanol, and 140 mL of hexane. The homogeneous solution was heated at 60 °C for 4 h. The upper layer containing the iron oleate complex was then washed thrice with 100 mL of distilled water in a separatory funnel. Excess hexane was removed by reduced-pressure distillation to purify iron oleate. The obtained iron oleate was mixed with 3.0 g of oleic acid and 100 g of 1-octadecene and then heated at 320 °C for 30 min at a rate of 3.3 °C/min under nitrogen atmosphere. After cooling down, Fe nanoparticles were

precipitated by adding 250 mL of ethanol to the solution and then separated by centrifugation. The products were washed several times with a mixture of hexane and ethanol and finally dispersed in 200 mL of hexane. The nanoparticles synthesized were uniform $\gamma$-$Fe_2O_3$ nanoparticles with a diameter of about 8.1 nm, as confirmed by XRD and TEM results (see Figs. S1 and S2). ICP results confirmed that no other elements (such as residual Na) were detected. $\alpha$-$Al_2O_3$ supports were prepared by calcination of AlOOH·$n$H$_2$O at 1200 °C for 4 h under air atmosphere. To load 10 wt. % Fe onto the $\alpha$-$Al_2O_3$ supports, 1.0 g of $\alpha$-$Al_2O_3$ was added into 100 mL of the above prepared hexane solution containing Fe nanoparticles, followed by stirring at room temperature for 24 h. Hexane was removed by rotary evaporation. The dried catalysts were then calcined at 350 °C for 4 h under air atmosphere, denoted as $Fe/Al_2O_3$.

## Preparation of Catalysts with Different Fe–Zn Proximities

To obtain a series of Fe–Zn bimetallic catalysts with changeable Fe–Zn distance, Fe and Zn nanoparticles were separately prepared to load. ZnO nanoparticles were also fabricated by thermal decomposition as previously described, in which 6.5 g of ferric chloride was changed to 5.5 g of zinc chloride. The size of the ZnO nanoparticles obtained was approximately 17.6 nm, as confirmed by XRD and TEM results (Figs. S1 and S2). Additionally, no residual Na was detected in ZnO, as confirmed by ICP analysis. The prepared Fe and Zn nanoparticles were then loaded onto the $\alpha$-$Al_2O_3$ supports by different methods. Specifically, the nanoparticles ($n_{Fe}$:$n_{Zn}$ = 1) were together dispersed in hexane and mixed with $\alpha$-$Al_2O_3$, followed by stirring at room temperature for 24 h. The suspension was dried by rotary evaporation, and it was then calcined at 350 °C for 4 h under static air, named $Fe_1Zn_1$-imp. Another, the prepared Fe and Zn nanoparticles were separately loaded on $\alpha$-$Al_2O_3$ and dried and calcined under the same conditions as previously described. The obtained $Fe/Al_2O_3$ and $Zn/Al_2O_3$ ($n_{Fe}$:$n_{Zn}$ = 1) were then physically mixed, named $Fe_1Zn_1$-mix. To further shorten the Fe–Zn distance, zinc nitrate solution was added into the prepared Fe nanoparticles in hexane solution and impregnated onto 1.0 g of $\alpha$-$Al_2O_3$, named $Fe_1Zn_1$-ion. The theoretical Fe

loading remained constant at about 10 wt. % for all catalysts. Figure 1 shows the schematic diagram of the fresh catalysts.

## Catalyst Characterizations

XRD patterns were measured by a SmartLab powder diffractometer with Cu K$\alpha$ radiation ($\lambda = 0.154$ nm) at 60 kV and 220 mA. The samples were tested at a scanning speed of 8°/min in the $2\theta$ range of 10–90°.

The specific surface area and pore structure properties of the catalysts were determined using a Micromeritics TriStar 3000 analyzer at $-196$ °C. The specific surface area and pore size distributions of the catalysts were calculated by the Brunauer–Emmet–Teller and Barrett–Joyner–Halenda methods, respectively. Before testing, the catalysts were evacuated at 200 °C for 3 h to remove impurities and moisture adsorbed on the surface.

An inductively coupled plasma optical emission spectrometer (ICP-OES, Thermo iCAP 7400) was used to analyze the elemental content of Fe and Zn in the samples. Before measurements, the samples were dissolved in a solution of HCl, $HNO_3$, and $H_3PO_4$ (volume ratio of 3: 1: 1) and treated at 200 °C for 4 h in a Teflon-lined stainless-steel autoclave.

The morphology and particle size of the samples were characterized by TEM spectroscopy (JEM-F200) at 200 kV. The particle size distribution was obtained by randomly measuring more than 300 nanoparticles in different regions. In the dark field, energy-dispersive X-ray (EDX)-mapping analysis was performed to obtain the elemental distribution.

$H_2$-TPR was conducted on a Micromeritics AutoChem II 2920 with a thermal conductivity detector (TCD). 50 mg of the fresh catalyst was pretreated in Ar flow at 200 °C for 1 h. The gas was then switched to a mixture of $H_2$ and Ar (10% $H_2$/90% Ar). The sample was heated from 50 to 800 °C at a rate of 10 °C/min, during which the signal was recorded using the TCD.

XPS measurements were collected using a Thermo Fisher ESCALAB 250Xi XPS instrument with an Al K$\alpha$ excitation source. The samples were tested in the vacuum with $5 \times 10^{-8}$ Pa. The binding energy was calibrated by selecting as the reference the C 1 s photoelectron peak at 284.8 eV.



**Fig. 1** Schematic diagram of **a** $Fe_1Zn_1$-ion, **b** $Fe_1Zn_1$-imp, **c** $Fe_1Zn_1$-mix, and **d** $Fe/Al_2O_3$ catalysts
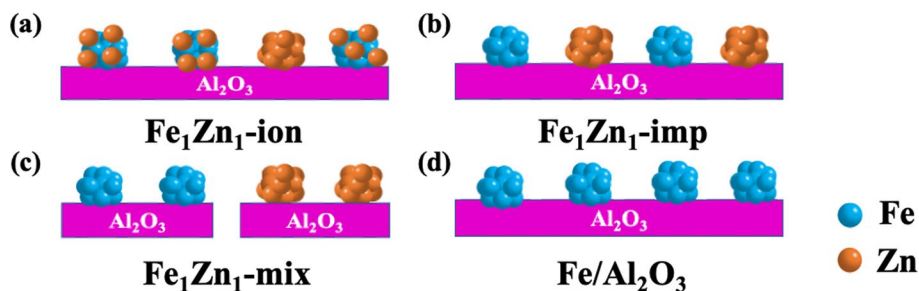
The graphitization degree of carbon species in spent catalysts was tested using a Raman spectrometer system (LabRAM HR Evolution, HORIBA Scientific) equipped with 532-nm laser excitation. The scanning range was 900–2000 $cm^{-1}$, and the resolution was set to 1.838 $cm^{-1}$.

[57]Fe Mössbauer spectroscopy was performed at -267 °C using a WSS-10 spectrometer controlled by Wissoft 2003 and a proportional counter (MFD-500AV, Japan) using [57]Co(Rh) as a γ-ray radioactive source. The temperature was controlled using JANIS Cryostat SHI-850–5. The velocity was calibrated using a standard α-Fe foil at − 267 °C. The components of the Fe-based phase were identified by fitted hyperfine parameters, including isomer shift (IS), quadruple splitting (QS), and magnetic hyperfine field (H). The compositions of the Fe-based phase were obtained based on the areas of γ photon adsorption peaks, assuming that the Fe nuclei had the same adsorption probability.

$CO_2$ temperature-programmed oxidation ($CO_2$-TPO) was conducted on a Micromeritics AutoChem II 2920 instrument connected with a quadrupole mass spectrometry (MS) instrument. The catalysts were activated online with CO gas at 350 °C for 5 h. The activated samples were then purged with pure Ar for 1 h to remove excess CO. After the activated samples were cooled down to room temperature, the gas was switched to a 10% $CO_2$/Ar mixture. The samples were heated from 50 to 800 °C at a rate of 10 °C/min, during which the signals were recorded using the MS instrument. $H_2$ temperature-programmed desorption ($H_2$-TPD) was conducted in the same facility. The catalysts were first reduced with 10% $H_2$/Ar at 350 °C for 5 h and then purged by Ar flow. After the catalysts were cooled down to room temperature, a 10% $H_2$/Ar gas mixture was introduced into the samples for 60 min. The MS signals were recorded upon heating the samples from 25 to 800 °C at a heating rate of 10 °C/min under Ar atmosphere.

## Catalyst Tests

The catalytic performance in a fixed-bed reactor was observed. In a typical test, 200 mg of a catalyst was added to the tubular reactor (inner diameter: 8.0 mm). The catalyst was reduced in situ with $H_2$ (30 mL/min) at 350 °C under 0.1 MPa for 5 h. The temperature was then reduced to 340 °C, and the pressure was adjusted to 2.0 MPa by

introducing Ar into the reactor. The space velocity of the catalyst was 9000 mL/(g·h), and the volume ratio of the gas mixture was 67.5% $H_2$/22.5% $CO_2$/10% Ar.

The gaseous products and residual reactants were analyzed using an online gas chromatograph (Agilent 7890B). Specifically, permanent gas and $CO_2$ were separated on an UltiMetal column and quantified using a TCD with Ar as an internal standard. $C_1$–$C_6$ hydrocarbons were separated on an HP-AL/S column and detected using a flame ionization detector.

$CO_2$ conversion was calculated using the following equation: $CO_2$ conv. = $(F_{CO2,in} − F_{CO2,out}) / F_{CO2,in}$. CO selectivity was calculated by the following equation: CO selectivity = (Moles of $CO_2$ converted to CO) / (Moles of input $CO_2$ − Moles of output $CO_2$). Selectivities to hydrocarbons were calculated on a carbon basis except for CO. Additionally, the activity of the catalysts was also expressed in terms of Fe time yield (FTY), meaning the moles of $CO_2$ converted to hydrocarbons per gram of Fe per second:

$$FTY = \frac{\text{Moles of } CO_2 \text{ converted to hydrocarbons}}{\text{Mass of Fe atoms} \times \text{Time}}$$

## Results and Discussion

### Properties of the as-Prepared Catalysts

The proximity between $Fe_2O_3$ and ZnO nanoparticles was examined by TEM equipped with EDX. As shown in Fig. 2a, $Fe_2O_3$ nanoparticles were uniformly deposited on the surface of α-$Al_2O_3$. In parallel, $Fe_2O_3$ and ZnO nanoparticles were observed to disperse over the α-$Al_2O_3$ surface with different distances for Fe–Zn bimetallic catalysts (see Fig. 2b–d). For $Fe_1Zn_1$-ion, the particle size was mainly centered at about 10 nm, which remained the same as the diameter of $Fe_2O_3$ nanoparticle precursors. However, for the $Fe_1Zn_1$-imp and $Fe_1Zn_1$-mix catalysts, $Fe_2O_3$ and ZnO nanoparticles were separated by a certain distance, whereas the ZnO nanocrystal was more adjacent to the $Fe_2O_3$ nanocrystal for $Fe_1Zn_1$-imp (see Fig. 2c–d). The proximity between Fe and Zn was further demonstrated by the EDX elemental mapping images of both fresh and spent catalysts (see Fig. 3 and Fig. S3).



Fig.2 TEM images of fresh catalysts: a Fe/$Al_2O_3$, b $Fe_1Zn_1$-ion, c $Fe_1Zn_1$-imp, and d $Fe_1Zn_1$-mix
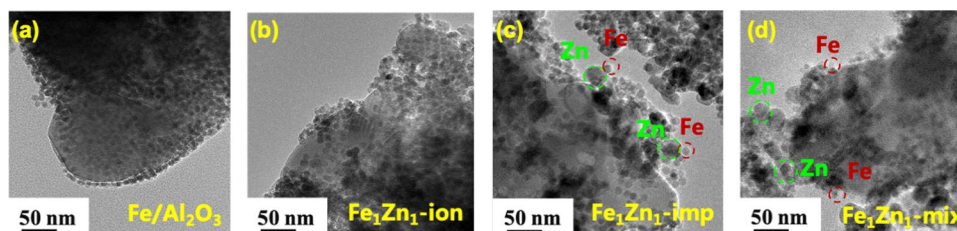
**Fig.3** EDX elemental mapping images of spent catalysts: **a** Fe$_1$Zn$_1$-ion, **b** Fe$_1$Zn$_1$-imp, and **c** Fe$_1$Zn$_1$-mix. **d** High-angle annular dark-field scanning transmission electron microscopy image and EDS line scanning of the spent Fe$_1$Zn$_1$-mix catalyst
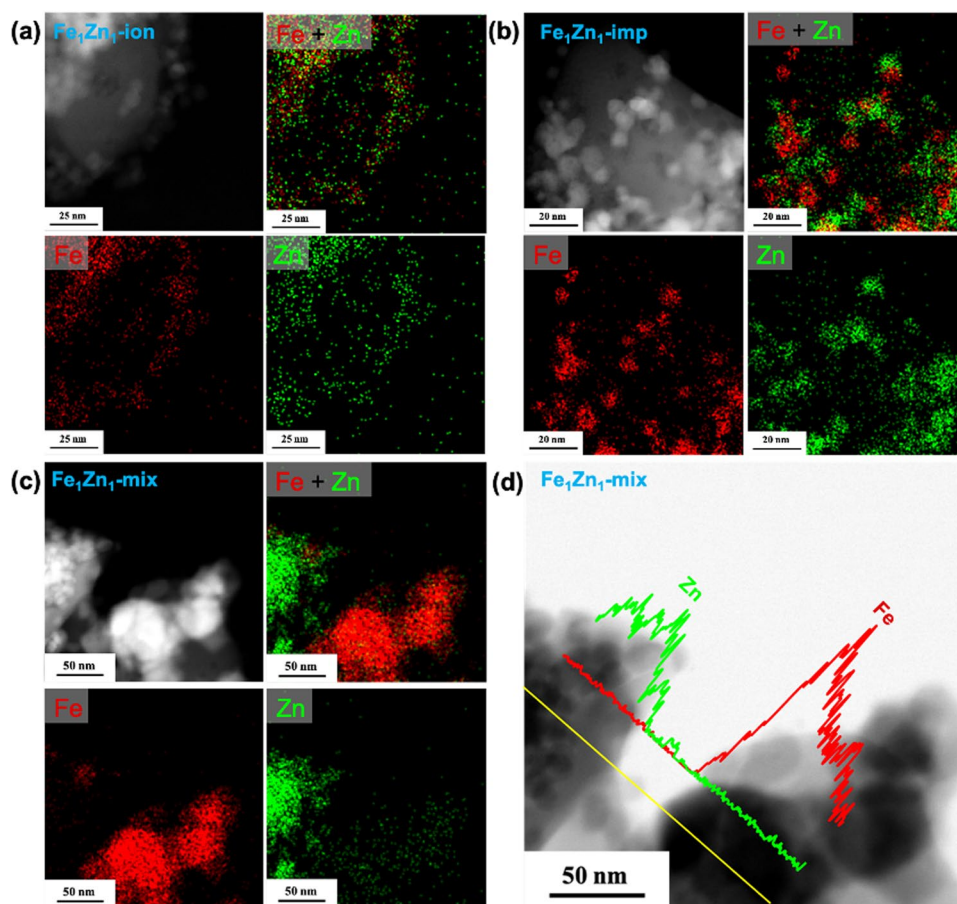


Both fresh and spent Fe$_1$Zn$_1$-ion samples exhibited a highly uniform and overlapping distribution of elements, indicating a close proximity between Fe and Zn. However, the elemental distribution of Fe and Zn in the Fe$_1$Zn$_1$-imp samples did not completely overlap (see Fig. 3b and Fig. S3b). The Fe and Zn elements became to enrich in certain regions. This suggested that a certain distance existed between Fe$_2$O$_3$ and ZnO particles in the catalyst. For the sample prepared by separate impregnation and physical mixing (Fe$_1$Zn$_1$-mix), Fe and Zn elements were obviously located at different regions (see Fig. 3c and Fig. S3c). Line scanning images further demonstrated that Fe and Zn elements clearly appeared in separate regions. This indicated that the distance between Fe$_2$O$_3$ and ZnO particles was farthest in the Fe$_1$Zn$_1$-mix catalyst. Notably, the proximity between Fe$_2$O$_3$ and ZnO for all the catalysts remained stable even after the reaction. Thus, the Fe–Zn bimetallic catalysts could be ranked on the basis of the relative distance between Fe$_2$O$_3$ and ZnO particles: Fe$_1$Zn$_1$-ion < Fe$_1$Zn$_1$-imp < Fe$_1$Zn$_1$-mix.

Fe-catalyzed CO$_2$ hydrogenation included the RWGS and FTS reactions [25–27]. The latter is a structure-sensitive reaction in which the particle size of the Fe species is critical in catalytic performance [25]. As the series of Fe and Fe–Zn catalysts retained the same size of Fe nanoparticles derived from the thermal decomposition method, the impact of size effect on the performance could be eliminated. Additionally, the data presented in Table S1 showed that the specific surface areas of the catalysts were almost the same and that the bimetallic catalysts were composed of Fe (about 9 wt.%) and Zn (about 10 wt.%) in a molar ratio of about 1 (see Table S1). Therefore, the bimetallic Fe–Zn model catalysts have been successfully prepared for solely investigating the Fe–Zn proximity effect on CO$_2$ hydrogenation.

The XRD patterns of fresh Fe/Al$_2$O$_3$, Fe$_1$Zn$_1$-ion, Fe$_1$Zn$_1$-imp, and Fe$_1$Zn$_1$-mix catalysts are shown in Fig. 4. The diffraction peaks at 30.3°, 35.7°, and 63.0° were assigned to γ-Fe$_2$O$_3$ (JCPDS 25-1402). The nature of the Fe species was further confirmed by the Fe 2p spectra (see Fig. S4). The satellite peak that appeared at ~719.0 eV could be assigned to the Fe$_2$O$_3$ species [28]. Additionally, compared with Fe/Al$_2$O$_3$, the diffraction peaks of Fe$_1$Zn$_1$-imp and Fe$_1$Zn$_1$-mix at about 63° were shifted toward lower angles. This was ascribed to the stacking of the ZnO phase, which held a lower characteristic diffraction peak. However, for Fe$_1$Zn$_1$-ion, the shift became more apparent, indicating Zn was partially inserted into the lattice of γ-Fe$_2$O$_3$. Conversely, close contact between Zn and Fe was achieved for Fe$_1$Zn$_1$-ion.

**Fig. 4** XRD patterns of freshFe$_1$Zn$_1$-ion, Fe$_1$Zn$_1$-imp, and Fe$_1$Zn$_1$-mix catalysts
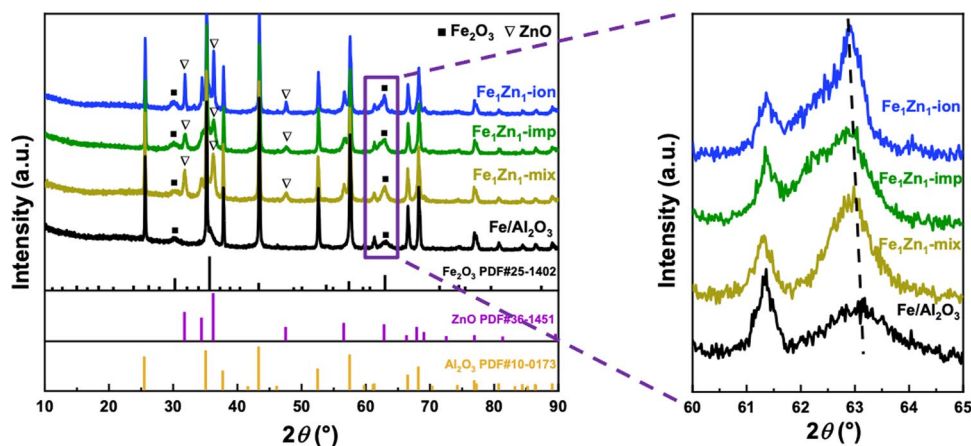
H$_2$-TPR was applied to analyze the interaction between Fe and Zn. As seen in Fig. 5a, the reduction temperature of Fe$_1$Zn$_1$-ion was higher than that of Fe$_1$Zn$_1$-imp and Fe$_1$Zn$_1$-mix. Additionally, Fe/Al$_2$O$_3$ was most prone to be reduced. This illustrates that Zn addition inhibits iron oxide reduction; the trend became increasingly obvious with closer Fe–Zn proximity. XRD patterns of the reduced catalysts are shown in Fig. 5b. The predominant ion phase of all the reduced catalysts was metallic Fe, which was evidenced by the intense diffraction peak located at 44.7°. Among the catalysts, the Fe/Al$_2$O$_3$ one exhibited the strongest diffraction peak of Fe, indicative of a high reduction degree under H$_2$ treatment. Along with ZnO addition and further shortening Fe–Zn distance, the intensity of Fe diffraction peaks was gradually weakened. Noteworthily, the diffraction peak of FeO appeared on Fe$_1$Zn$_1$-ion. This indicated that the inhibition of Fe reduction would become prominent because of the closest proximity between Fe and Zn, in accordance with the H$_2$-TPR results. Moreover, for reduced Fe–Zn bimetallic catalysts, no angle shift was observed compared with the characteristic peaks of

metallic Fe-based catalysts, indicating the reduced catalysts did not contain the Fe–Zn alloy phase.

## Catalytic Performance

To understand the effect of Fe–Zn proximity on CO$_2$ hydrogenation performance, catalysts with different Fe–Zn distances were evaluated. As presented in Table 1, CO$_2$ conversions on the Fe–Zn bimetallic catalysts were all higher than that on the Fe catalyst without a promoter due to the promotion effect of ZnO on the RWGS reaction [13]. By physically mixing ZnO/Al$_2$O$_3$ with Fe/Al$_2$O$_3$, the activity increased from 32.7% to 42.7%. Shortening the Fe–Zn distance (i.e., Fe$_1$Zn$_1$-imp) further improved the activity with almost identical CO selectivity. This demonstrated that a relatively closer distance between Fe and Zn contributed to enhancing the RWGS and FTS reactions. However, for the Fe$_1$Zn$_1$-ion sample, CO$_2$ conversion turned to decrease, along with a remarkably increased CO selectivity. This indicated that the FTS reaction was obviously inhibited over Fe$_1$Zn$_1$-ion, then hindering the forward reaction of RWGS.



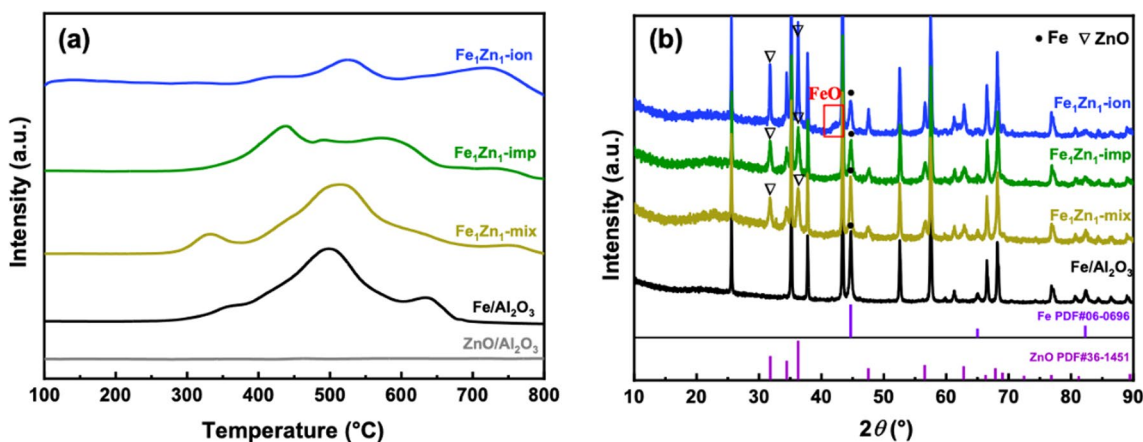**Fig. 5** **a** H$_2$-TPR profiles of Fe/Al$_2$O$_3$, Fe$_1$Zn$_1$-ion, Fe$_1$Zn$_1$-imp, and Fe$_1$Zn$_1$-mix catalysts; **b** XRD patterns of the reduced catalysts

**Table 1** Catalytic performance of $Fe_1Zn_1$-ion, $Fe_1Zn_1$-imp, $Fe_1Zn_1$-mix, and $Fe/Al_2O_3$ catalysts

| Catalysts | $CO_2$ conv. (%) | FTY ($\mu mol_{CO2}$ $g_{Fe}^{-1} s^{-1}$) | CO selectivity (%) | Hydrocarbon selectivity (C-mol%) | | | |
|---|---|---|---|---|---|---|---|
| | | | | $CH_4$ | $C_2$–$C_4$ | $C_{5+}$ | Oxy |
| $Fe_1Zn_1$-ion | 35.4 | 77 | 28.2 | 27.4 | 18.6 | 53.8 | 0.2 |
| $Fe_1Zn_1$-imp | 44.7 | 120 | 12.5 | 27.5 | 24.6 | 47.5 | 0.4 |
| $Fe_1Zn_1$-mix | 42.7 | 113 | 12.1 | 26.4 | 25.9 | 47.3 | 0.4 |
| $Fe/Al_2O_3$ | 32.7 | 81 | 11.6 | 39.1 | 29.8 | 30.8 | 0.3 |

Reaction conditions: 0.2 g cat., 340 °C, 2.0 MPa, $H_2/CO_2 = 3$, GHSV = 9000 mL/(g·h), TOS = 60 h

The changes in activity and CO selectivity caused by controllable Fe–Zn distances revealed that suitable proximity can simultaneously facilitate the RWGS and FTS reactions.

The distribution of hydrocarbon products showed that the Fe–Zn bimetallic catalysts exhibited lower $CH_4$ selectivity and higher $C_{5+}$ selectivity than $Fe/Al_2O_3$. This indicated that the addition of ZnO promoted the C–C coupling process and shifted the product distribution toward hydrocarbons with a higher number of carbon atoms. Reportedly, the presence of ZnO increases the intensity of $–CH_3$ or $–CH_2$ groups, which are important intermediates for C–C coupling [29]. The $Fe_1Zn_1$-ion catalyst exhibited the highest $C_{5+}$ selectivity, suggesting that a closer distance between Fe and Zn further promoted C–C coupling. $H_2$-TPD profiles in Fig. S5 show that the series of Fe–Zn bimetallic catalysts had a lower temperature of $H_2$ desorption in comparison with $Fe/Al_2O_3$, illustrating the weakened $H_2$ adsorption caused by Zn addition. Consequently, the formation of $CH_4$ and $C_{2–4}$ hydrocarbons was suppressed. Within 60 h of the catalyst tests, $Fe/Al_2O_3$ exhibited a relatively apparent deactivation behavior (Fig. 6). However, the $CO_2$ conversion on the stream became more stable over time upon introducing Zn as a promoter. Particularly for the $Fe_1Zn_1$-ion catalyst, the activity even became almost constant after 10 h. Therefore, with the decrease in distance between Fe and Zn, the stability was further improved.

## Structure–Performance Relationship

During the $CO_2$ hydrogenation reaction, the reduced Fe catalyst undergoes carburization and oxidation. Finally, the Fe phases of the spent catalysts exist in the form of $Fe_3O_4$ and $Fe_5C_2$ (see Fig. 7), which are, respectively, regarded as the active phases for the RWGS and FTS reactions [6, 30, 31]. The Zn phases still existed in the form of ZnO. XPS was performed to determine the surface phase compositions of the spent catalysts (see Fig. 8a). Deconvolution of the Fe 2p spectra revealed two peaks appearing at approximately 707.5 and 710.5 eV, which could be, respectively, assigned to $Fe_5C_2$ and $Fe_3O_4$ [32–35]. Among all the spent catalysts, the $Fe/Al_2O_3$ catalyst exhibited the highest peak area ratio of $Fe_5C_2/Fe_3O_4$ (0.78), followed by the $Fe_1Zn_1$-mix (0.56) and $Fe_1Zn_1$-imp (0.45) catalysts.
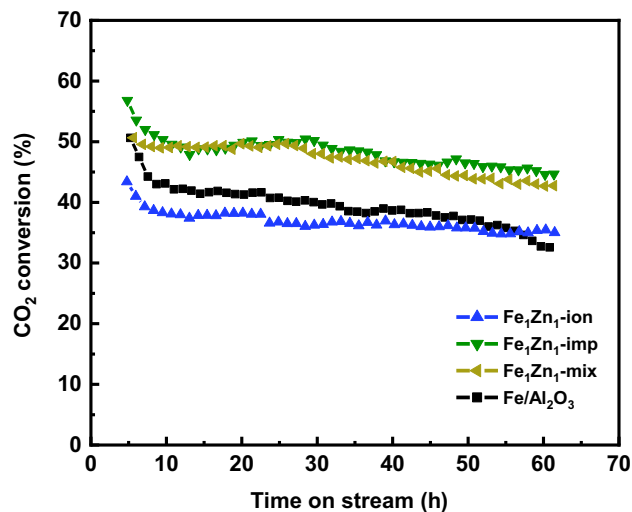


**Fig. 6** $CO_2$ conversion on time on stream for the $Fe_1Zn_1$-ion, $Fe_1Zn_1$-imp, $Fe_1Zn_1$-mix, and $Fe/Al_2O_3$ catalysts
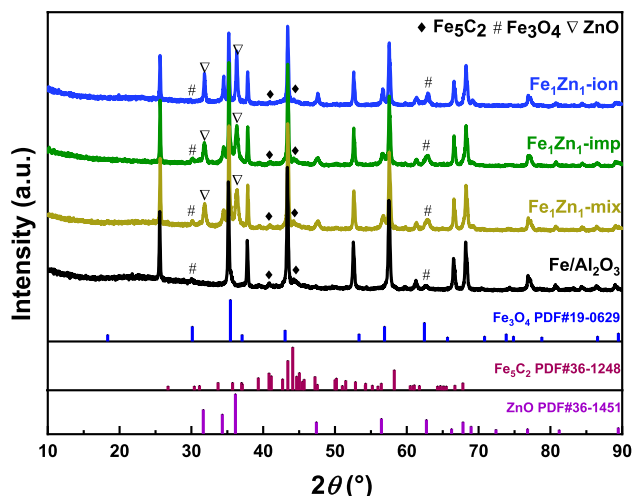


**Fig. 7** XRD patterns of the spent catalysts

However, the $Fe_1Zn_1$-ion catalyst exhibited the lowest ratio (0.29). This means that the addition of Zn led to a decrease in the ratio of $Fe_5C_2$ to $Fe_3O_4$ and that as the Fe–Zn distance became smaller, more $Fe_3O_4$ formed during the
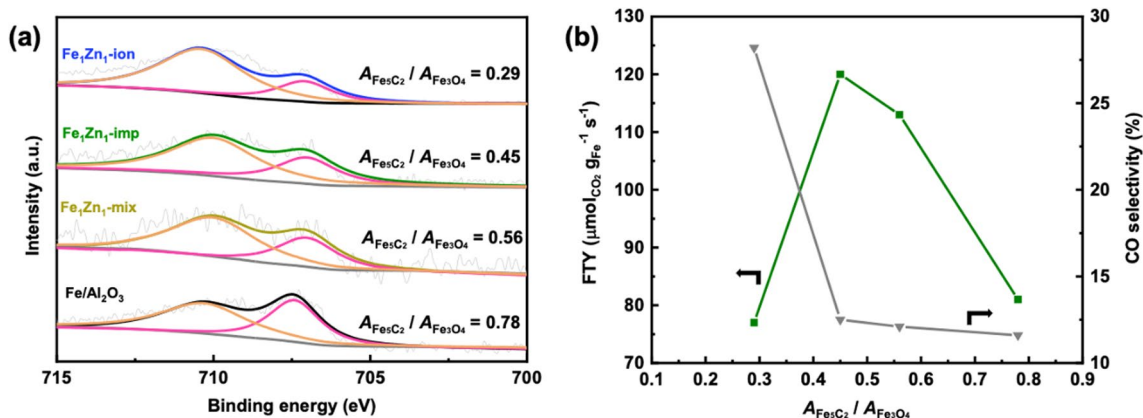
**Fig. 8** **a** XPS patterns of the spent catalysts and **b** FTY and CO selectivity as a function of the ratio of $Fe_5C_2$ and $Fe_3O_4$

reaction. Generally, $Fe_3O_4$ was the active phase for catalyzing the RWGS reaction, while $Fe_5C_2$ was responsible for CO hydrogenation. Figure 8b shows the relationship between the ratio of $Fe_5C_2$ and $Fe_3O_4$ and the reaction properties. FTY initially increased and then decreased as the ratio increased from 0.29 to 0.78. However, CO selectivity initially decreased and then remained almost unchanged with an increasing ratio. Considering the reversible characteristic of the RWGS reaction, expediting CO conversion would push the reaction equilibrium shift toward CO production, according to Le Chatelier's Principle. Therefore, a balance should be established between RWGS and FTS performances. In this case, the $Fe_1Zn_1$-ion catalyst held a relatively higher $Fe_3O_4$ content but a lower $Fe_5C_2$ content; hence, the CO formed cannot be converted to hydrocarbons in time. The reaction equilibrium was the main limiting factor. For the $Fe_1Zn_1$-imp catalyst, a proper proportion of $Fe_3O_4$ and $Fe_5C_2$ enabled the timely conversion of CO intermediates generated by the RWGS

reaction. Consequently, a superior activity was obtained on the $Fe_1Zn_1$-imp catalyst.

To further quantify the composition of the different Fe phases, the spent catalysts were characterized by Mössbauer spectroscopy (see Fig. 9a). The corresponding data are presented in Table 2. The patterns were fitted with 5 sextets. The 3 sextets with an H value of approximately 25 T, 22 T, and 13 T were attributed to $\chi$-$Fe_5C_2$ and the 2 sextets with H of approximately 51 and 45 T corresponded to $Fe_3O_4$ [36]. The $Fe/Al_2O_3$ catalyst had the highest mass ratio of $Fe_5C_2$ to $Fe_3O_4$ in bulk phases, indicating that it was more prone to be carburized during the reaction. This is in line with the $H_2$-TPR result (see Fig. 5a), in which $Fe/Al_2O_3$ was most easily reduced. After ZnO introduction, the content of $Fe_5C_2$ in bulk phases tended to decrease, demonstrating that the addition of ZnO inhibited the carburization of Fe. Additionally, as the Fe–Zn proximity increased, carburization of the Fe species was gradually suppressed, leading to a lower content of $Fe_5C_2$. To observe the oxidization degree of the fully carburized catalysts with different Fe–Zn distances by
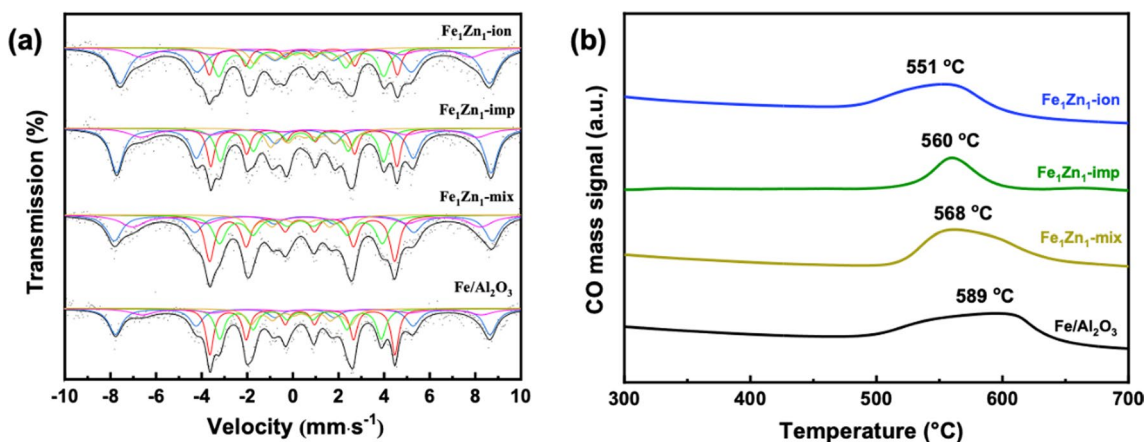


**Fig. 9** **a** $^{57}$Fe Mössbauer spectra of the spent catalysts measured at $-267$ °C and **b** $CO_2$-TPO profiles of the activated catalysts

**Table 2** $^{57}$Fe Mössbauer parameters of the spent catalysts

| Spent catalysts | IS (mm·s$^{-1}$) | QS (mm·s$^{-1}$) | $H$ (T) | Phase ascription | Relative area (%) |
|---|---|---|---|---|---|
| Fe$_1$Zn$_1$-ion | 0.51 | 0.02 | 50.4 | Fe$_3$O$_4$(A) | 39.6 |
| | 0.58 | 0.01 | 44.9 | Fe$_3$O$_4$(B) | 14.8 |
| | 0.40 | 0.13 | 25.7 | χ-Fe$_5$C$_2$(A) | 14.2 |
| | 0.30 | 0.14 | 22.5 | χ-Fe$_5$C$_2$(B) | 21.2 |
| | 0.44 | − 0.03 | 13.2 | χ-Fe$_5$C$_2$(C) | 10.2 |
| Fe$_1$Zn$_1$-imp | 0.50 | − 0.04 | 51.0 | Fe$_3$O$_4$(A) | 36.0 |
| | 0.72 | 0.01 | 45.8 | Fe$_3$O$_4$(B) | 13.6 |
| | 0.41 | 0.14 | 25.4 | χ-Fe$_5$C$_2$(A) | 18.5 |
| | 0.37 | 0.05 | 22.3 | χ-Fe$_5$C$_2$(B) | 20.3 |
| | 0.79 | − 0.03 | 10.9 | χ-Fe$_5$C$_2$(C) | 11.6 |
| Fe$_1$Zn$_1$-mix | 0.48 | − 0.05 | 51.5 | Fe$_3$O$_4$(A) | 24.1 |
| | 0.59 | 0.01 | 47.4 | Fe$_3$O$_4$(B) | 17.5 |
| | 0.36 | 0.10 | 25.2 | χ-Fe$_5$C$_2$(A) | 26.9 |
| | 0.34 | 0.03 | 22.2 | χ-Fe$_5$C$_2$(B) | 21.6 |
| | 0.33 | − 0.03 | 13.5 | χ-Fe$_5$C$_2$(C) | 9.9 |
| Fe/Al$_2$O$_3$ | 0.50 | − 0.08 | 51.0 | Fe$_3$O$_4$(A) | 26.6 |
| | 0.85 | 0.01 | 46.2 | Fe$_3$O$_4$(B) | 11.8 |
| | 0.39 | 0.11 | 25.2 | χ-Fe$_5$C$_2$(A) | 26.6 |
| | 0.35 | 0.02 | 22.0 | χ-Fe$_5$C$_2$(B) | 22.2 |
| | 0.38 | − 0.03 | 13.6 | χ-Fe$_5$C$_2$(C) | 12.8 |

an oxidant (CO₂), CO₂-TPO of the CO-treated catalysts was conducted (see Fig. 9b). As shown in Fig. S6, all the CO-treated catalysts existed in the χ-Fe₅C₂ phase. Compared with the Fe/Al₂O₃ catalyst, the Fe–Zn bimetallic catalysts exhibited a lower oxidation temperature. This trend continued to become stronger with further shortening of the distance between the Fe and Zn. Therefore, adding a Zn promoter and modulating the Fe–Zn proximity affect the reduction of Fe oxides and oxidation of carbides, ultimately regulating the composition of Fe₅C₂ and Fe₃O₄.

Figure 10 shows the Raman spectra of the spent catalysts. All the spent catalysts exhibited two main bands at approximately 1340 and 1580 cm$^{-1}$, which represented the D band (structural disorders) and G band (graphitized carbon), respectively [37–39]. The ratio of the D band to the G band ($I_D/I_G$) is typically used as an indicator to describe the graphitization degree. A higher $I_D/I_G$ ratio indicates more defects and a higher disordered structure of carbon deposit on the surface. Compared with the Fe–Zn bimetallic catalysts, the Fe/Al₂O₃ catalyst held a lower $I_D/I_G$ value, indicating that more graphite carbon deposits were formed during the reaction. Accordingly, a thick carbon layer could be seen in the TEM image of the spent Fe/Al₂O₃ catalyst (see Fig. S7). The graphitic carbon layer would block active phases and lead to catalyst deactivation, consistent with its poor stability (see Fig. 6). After the Zn introduction, the $I_D/I_G$ value tended to
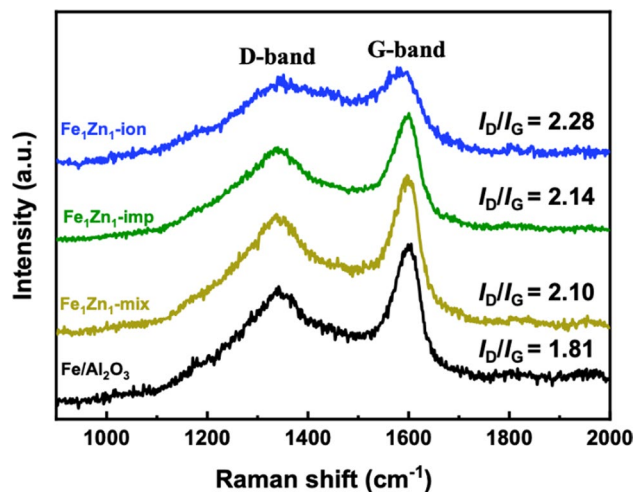


**Fig. 10** Raman spectra of the spent catalysts

increase, demonstrating that the presence of Zn inhibited the formation of graphite carbon. Noteworthily, the spent Fe₁Zn₁-ion catalyst had the highest $I_D/I_G$; additionally, the carbon layer was merely observed in the TEM images of the spent Fe₁Zn₁-ion catalyst. Hence, high proximity between Fe and Zn could further inhibit carbon deposition during the reaction and improve catalyst stability.

## Conclusions

A series of Fe–Zn bimetallic catalysts with different Fe–Zn proximities were obtained by tuning the impregnation sequence or mixing method. Upon adding Zn and further shortening the Fe–Zn distance, the reduction of the Fe species exhibited a gradually suppressed tendency. The composition analysis of the Fe phases revealed that the interaction of Zn and Fe inhibited the carburization of the Fe species and promoted the oxidization of carbides during the reaction. A volcano-type relationship between the catalytic activity and the ratio of $Fe_5C_2$ and $Fe_3O_4$ was observed. Additionally, the $Fe_1Zn_1$-imp catalyst with a medium ratio of $Fe_5C_2$ and $Fe_3O_4$ content simultaneously contributed to the RWGS reaction and CO hydrogenation, thus facilitating the entire $CO_2$ hydrogenation reaction. Meanwhile, adding Zn and further reducing the Fe–Zn distance promoted the C–C coupling process, resulting in higher $C_{5+}$ selectivity. Compared with the $Fe_2O_3/Al_2O_3$ catalyst, the Fe-Zn bimetallic catalysts exhibited higher catalytic stability. Particularly, close proximity between Zn and Fe species was observed to inhibit carbon deposition. The design of this model catalyst provided a novel way of studying the proximity effects for bimetallic catalysts. Additionally, it enriched the understanding of the relationship between the composition and activity of active phases ($Fe_5C_2$ and $Fe_3O_4$) in Fe-catalyzed $CO_2$ hydrogenation reactions.

## Declarations

**Conflicts of interest** Xinbin Ma is an editorial board member for *Transactions of Tianjin University* and was not involved in the editorial review or the decision to publish this article. All authors declare that there are no competing interests.

## References

1. De S, Dokania A, Ramirez A et al (2020) Advances in the design of heterogeneous catalysts and thermocatalytic processes for $CO_2$ utilization. ACS Catal 10(23):14147–14185

2. Yang Q, Skrypnik A, Matvienko A et al (2021) Revealing property-performance relationships for efficient $CO_2$ hydrogenation to higher hydrocarbons over Fe-based catalysts: statistical analysis of literature data and its experimental validation. Appl Catal B Environ 282:119554

3. Liu XY, Pan YL, Zhang P et al (2022) Alkylation of benzene with carbon dioxide to low-carbon aromatic hydrocarbons over bifunctional Zn-Ti/HZSM-5 catalyst. Front Chem Sci Eng 16(3):384–396

4. Cheng Y, Lin J, Wu T et al (2017) Mg and K dual-decorated Fe-on-reduced graphene oxide for selective catalyzing CO hydrogenation to light olefins with mitigated $CO_2$ emission and enhanced activity. Appl Catal B Environ 204:475–485

5. Guo LS, Li J, Cui Y et al (2020) Spinel-structure catalyst catalyzing $CO_2$ hydrogenation to full spectrum alkenes with an ultra-high yield. Chem Commun 56(65):9372–9375

6. Pérez-Alonso FJ, Ojeda M, Herranz T et al (2008) Carbon dioxide hydrogenation over Fe-Ce catalysts. Catal Commun 9(9):1945–1948

7. Xu M, Liu X, Song G et al (2022) Regulating iron species compositions by Fe–Al interaction in $CO_2$ hydrogenation. J Catal 413:331–341

8. Hwang SM, Han SJ, Min JE et al (2019) Mechanistic insights into Cu and K promoted Fe-catalyzed production of liquid hydrocarbons via $CO_2$ hydrogenation. J $CO_2$ Util 34:522–532

9. Liu Y, Chen JF, Bao J et al (2015) Manganese-modified $Fe_3O_4$ microsphere catalyst with effective active phase of forming light olefins from syngas. ACS Catal 5(6):3905–3909

10. Liu Q, Ding J, Ji GJ et al (2021) Fe-Co-K/$ZrO_2$ catalytic performance of $CO_2$ hydrogenation to light olefins. J Inorg Mater 36(10):1053

11. Choi YH, Ra EC, Kim EH et al (2017) Sodium-containing spinel zinc ferrite as a catalyst precursor for the selective synthesis of liquid hydrocarbon fuels. Chemsuschem 10(23):4764–4770

12. Wang H, Yang Y, Xu J et al (2010) Study of bimetallic interactions and promoter effects of FeZn, FeMn and FeCr Fischer-Tropsch synthesis catalysts. J Mol Catal A Chem 326(1–2):29–40

13. Zhang Z, Yin H, Yu G et al (2021) Selective hydrogenation of $CO_2$ and CO into olefins over sodium- and zinc-promoted iron carbide catalysts. J Catal 395:350–361

14. Sai Prasad PS, Bae JW, Jun KW, Lee KW (2008) Fischer-Tropsch synthesis by carbon dioxide hydrogenation on Fe-based catalysts. Catal Surv Asia 12(3):170–183

15. Zhai P, Xu C, Gao R et al (2016) Highly tunable selectivity for syngas-derived alkenes over zinc and sodium-modulated $Fe_5C_2$ catalyst. Angew Chem Int Ed 55(34):9902–9907

16. Gao X, Zhang J, Chen N et al (2016) Effects of zinc on Fe-based catalysts during the synthesis of light olefins from the Fischer-Tropsch process. Chin J Catal 37(4):510–516

17. Zhang C, Cao CX, Zhang YL et al (2021) Unraveling the role of zinc on bimetallic $Fe_5C_2$-ZnO catalysts for highly selective carbon dioxide hydrogenation to high carbon α-olefins. ACS Catal 11(4):2121–2133

18. Cai W, Han HJ, Hu CY et al (2023) Fabrication of transition metal (Mn Co, Ni, Cu)-embedded faveolate $ZnFe_2O_4$ spinel structure with robust $CO_2$ hydrogenation into value-added C2+ hydrocarbons. ChemCatChem 15(6):e202201403

19. Zhang J, Lu S, Su X et al (2015) Selective formation of light olefins from $CO_2$ hydrogenation over Fe-Zn-K catalysts. J $CO_2$ Util 12:95–100

20. Xu MJ, Liu XL, Cao CX et al (2021) Ternary Fe-Zn-Al spinel catalyst for $CO_2$ hydrogenation to linear $\alpha$-olefins: synergy effects between Al and Zn. ACS Sustain Chem Eng 9(41):13818–13830

21. Malhi HS, Sun C, Zhang Z et al (2022) Catalytic consequences of the decoration of sodium and zinc atoms during $CO_2$ hydrogenation to olefins over iron-based catalyst. Catal Today 387:28–37

22. Ding HL, Zhang YX, Wang S et al (2012) $Fe_3O_4$@$SiO_2$ core/shell nanoparticles: the silica coating regulations with a single core for different core sizes and shell thicknesses. Chem Mater 24(23):4572–4580

23. Kim KY, Lee H, Noh WY et al (2020) Cobalt ferrite nanoparticles to form a catalytic Co-Fe alloy carbide phase for selective $CO_2$ hydrogenation to light olefins. ACS Catal 10(15):8660–8671

24. Park J, An K, Hwang Y et al (2004) Ultra-large-scale syntheses of monodisperse nanocrystals. Nat Mater 3(12):891–895

25. Yuan Y, Huang SY, Wang HY et al (2017) Monodisperse nano-$Fe_3O_4$ on $\alpha$-$Al_2O_3$ catalysts for Fischer-Tropsch synthesis to lower olefins: promoter and size effects. ChemCatChem 9(16):3144–3152

26. Han ZH, Qian WX, Ma HF et al (2020) Study of the Fischer-Tropsch synthesis on nano-precipitated iron-based catalysts with different particle sizes. RSC Adv 10(70):42903–42911

27. Zhao Q, Liang H, Huang S et al (2021) Tunable $Fe_3O_4$ nanoparticles assembled porous microspheres as catalysts for Fischer-Tropsch synthesis to lower olefins. Catal Today 368:133–139

28. Cheng Y, Lin J, Xu K et al (2016) Fischer-Tropsch synthesis to lower olefins over potassium-promoted reduced graphene oxide supported iron catalysts. ACS Catal 6(1):389–399

29. Zhang C, Xu M, Yang Z et al (2021) Uncovering the electronic effects of zinc on the structure of $Fe_5C_2$-ZnO catalysts for $CO_2$ hydrogenation to linear $\alpha$-olefins. Appl Catal B Environ 295:120287

30. Ronda-Lloret M, Rothenberg G, Shiju NR (2019) A critical look at direct catalytic hydrogenation of carbon dioxide to olefins. Chemsuschem 12(17):3896–3914

31. Wei J, Ge QJ, Yao RW et al (2017) Directly converting $CO_2$ into a gasoline fuel. Nat Commun 8:15174

32. Yamashita T, Hayes P (2008) Analysis of XPS spectra of $Fe^{2+}$ and $Fe^{3+}$ ions in oxide materials. Appl Surf Sci 254(8):2441–2449

33. Lu F, Chen X, Lei Z et al (2021) Revealing the activity of different iron carbides for Fischer-Tropsch synthesis. Appl Catal B Environ 281:119521

34. Lu F, Huang J, Wu Q et al (2021) Mixture of $\alpha$-$Fe_2O_3$ and $MnO_2$ powders for direct conversion of syngas to light olefins. Appl Catal A Gen 621:118213

35. Yang C, Zhao HB, Hou YL et al (2012) $Fe_5C_2$ nanoparticles: a facile bromide-induced synthesis and as an active phase for Fischer-Tropsch synthesis. J Am Chem Soc 134(38):15814–15821

36. Najarnia F, Ahmadpoor F, Sahebian S et al (2022) Thermal decomposition kinetic study of $Fe_5C_2$ nanoparticles. J Phys Chem Solids 161:110436

37. Cheng D, Zhao Y, An T et al (2019) 3D interconnected crumpled porous carbon sheets modified with high-level nitrogen doping for high performance lithium sulfur batteries. Carbon 154:58–66

38. Hamilton NG, Warringham R, Silverwood IP et al (2014) The application of inelastic neutron scattering to investigate CO hydrogenation over an iron Fischer-Tropsch synthesis catalyst. J Catal 312:221–231

39. Wei YX, Zhang CH, Liu X et al (2018) Enhanced Fischer-Tropsch performances of graphene oxide-supported iron catalysts via argon pretreatment. Catal Sci Technol 8(4):1113–1125

**Qiao Zhao** is a lecturer in School of Materials Science and Engineering at Nankai University. She studied chemical engineering and received her B.S. degree from Dalian University of Technology and her M.S. and Ph.D. degrees from Tianjin University. She then worked as a postdoctoral fellow at Tianjin University and Zhejiang Institute of Tianjin University collaborating with Professor Xinbin Ma. Her research focuses on the design and application of functional nanomaterials in catalysis, including Fe-catalyzed CO or $CO_2$ hydrogenation, electrochemical $CO_2$ reduction.
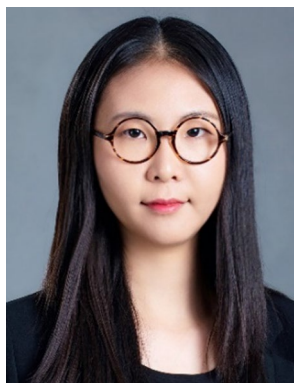


**Shouying Huang** obtained her Ph.D. degree in 2013 from TianjinUniversity. After a postdoctoral project in Nankai University, she joined TianjinUniversity as an associate professor in 2016 and was promoted to professor in 2022.Her research interest mainly focuses on heterogenous catalysis for efficient utilizationof C1 resources, including CO/$CO_2$ hydrogenation, carbonylation etc.